

# Chemical Science

Accepted Manuscript

This article can be cited before page numbers have been issued, to do this please use: M. Chen, H. Boström, D. Daisenberger, N. P. Funnell, C. J. Ridley and A. B. Cairns, *Chem. Sci.*, 2026, DOI: 10.1039/D5SC04854K.



This is an Accepted Manuscript, which has been through the Royal Society of Chemistry peer review process and has been accepted for publication.

Accepted Manuscripts are published online shortly after acceptance, before technical editing, formatting and proof reading. Using this free service, authors can make their results available to the community, in citable form, before we publish the edited article. We will replace this Accepted Manuscript with the edited and formatted Advance Article as soon as it is available.

You can find more information about Accepted Manuscripts in the [Information for Authors](#).

Please note that technical editing may introduce minor changes to the text and/or graphics, which may alter content. The journal's standard [Terms & Conditions](#) and the [Ethical guidelines](#) still apply. In no event shall the Royal Society of Chemistry be held responsible for any errors or omissions in this Accepted Manuscript or any consequences arising from the use of any information it contains.

Cite this: DOI: 00.0000/xxxxxxxxxx

## Negative and Zero Linear Compressibility in Copper Dicyanamide and Tricyanomethanide

Muzi Chen,<sup>\*abc</sup> Hanna L. B. Boström,<sup>de</sup> Dominik Daisenberger,<sup>f</sup> Nicholas P. Funnell,<sup>g</sup> Christopher J. Ridley,<sup>gh</sup> and Andrew B. Cairns<sup>\*ab</sup>Received Date  
Accepted Date

DOI: 00.0000/xxxxxxxxxx

Rutile-structured materials can exhibit negative linear compressibility (NLC) following ferroelastic phase transitions, expanding in one direction under uniform compression. We investigate this phenomenon in structural analogues—transition metal dicyanamides (dca) and tricyanomethanides (tcm) with single and double rutile-like structures, respectively. The pressure-induced structural behavior of Cu(tcm)<sub>2</sub> and Cu(dca)<sub>2</sub> are studied using high-pressure diffraction. Both systems undergo anisotropic deformation upon compression, with Cu(dca)<sub>2</sub> exhibiting NLC of  $-6.5(10)$  TPa<sup>-1</sup> along the *c*-axis, while Cu(tcm)<sub>2</sub> shows zero linear compressibility (ZLC) in the *a*-axis. This difference is attributed to the single rutile-like network with flexible dca<sup>-</sup> linkers in Cu(dca)<sub>2</sub>, in contrast to the more constrained doubly interpenetrating structure of Cu(tcm)<sub>2</sub> with rigid tcm<sup>-</sup> linkers. We also study the interplay between structural features and electronic effects arising from Jahn-Teller distortion of metal coordination in both materials, in controlling their compression behaviour.

## 1 Introduction

Negative linear compressibility (NLC) is the property of materials to increase in length along one direction when hydrostatically compressed.<sup>1</sup> This has attracted interest for potential applications in various fields, such as molecular-scale artificial muscles and pressure sensors.<sup>2</sup> To date, NLC has been identified in a wide variety of materials, including inorganic oxides, molecular solids, metal cyanides, and metal-organic frameworks (MOFs).<sup>3–7</sup> The most impressive NLC performances of existing materials are shown by metal cyanides. Their NLC mechanisms are based on the pressure-induced deformation of flexible frameworks. The rapid compression in one direction is transferred

to an expansion in the perpendicular direction via flexing of the framework. Two typical examples are Zn[Au(CN)<sub>2</sub>]<sub>2</sub> and Ag<sub>3</sub>[Co(CN)<sub>6</sub>] with flexible “honeycomb” and “wine-rack” frameworks, respectively.<sup>8,9</sup> Despite these advances, research efforts continue, aiming to uncover novel NLC materials with superior properties—such as larger compressibility magnitudes, broader pressure ranges of operation, or enhanced mechanical stability—or operating through alternative mechanisms. The ultimate goal is to gain a deeper understanding of the underlying principles that govern this exceptional property.

Rutile, one of the three crystalline polymorphs of titanium dioxide (TiO<sub>2</sub>), has a well-known tetragonal crystal structure composed of columns of edge-sharing TiO<sub>6</sub> octahedra (as shown in Figure 1).<sup>10,11</sup> This structure is ferroelastically unstable at high pressures or low temperatures due to the coordinated rotation of adjacent octahedral columns, resulting in a distorted orthorhombic CaCl<sub>2</sub>-like structure.<sup>12,13</sup> The main difference between these two polymorphs is the rotation of the edge-sharing octahedra around the *c*-axis, which breaks the 4-fold symmetry in CaCl<sub>2</sub>-like structures.<sup>14,15</sup> Several dioxides and difluorides with the rutile structure undergo similar phase transitions, with the resulting low-symmetric CaCl<sub>2</sub>-like phases exhibiting NLC in one of the orthogonal directions.<sup>16</sup> These transitions are directly responsible for inducing NLC in rutile-structured solids.

Furthermore, they are classified as proper ferroelastic transitions, with strain tensor components acting as primary order parameters.<sup>17,18</sup> This transition is associated with the softening of a B<sub>1g</sub> mode (ferroelastic instability) involving octahedral ro-

<sup>a</sup> Department of Materials, Imperial College London, Royal School of Mines, Exhibition Road, SW7 2AZ, London, UK. Tel: +44(0)20 7594 9528; E-mail: a.cairns@imperial.ac.uk

<sup>b</sup> London Centre for Nanotechnology, Imperial College London, London SW7 2AZ, UK.

<sup>c</sup> Present address: Department of Heterogeneous Catalysis, Max-Planck-Institut für Kohlenforschung, Kaiser-Wilhelm-Platz 1, D-45470 Mülheim an der Ruhr, Germany. Tel: +49(0)176 2873 6256; E-mail: muzichen@kofo.mpg.de

<sup>d</sup> Department of Chemistry, Stockholm University, Svante Arrhenius väg 16C, SE-106 91, Stockholm, Sweden.

<sup>e</sup> Wallenberg Initiative Materials Science for Sustainability, Department of Chemistry, Stockholm University, SE-114 18, Stockholm, Sweden.

<sup>f</sup> Diamond Light Source Ltd., Harwell Campus, Didcot OX11 0DE, UK.

<sup>g</sup> ISIS Neutron and Muon Source, Rutherford Appleton Laboratory, Harwell Campus, Didcot OX11 0QX, UK.

<sup>h</sup> Present address: Neutron Scattering Division, Oak Ridge National Laboratory, Oak Ridge, TN 37831, USA.

† Electronic Supplementary Information (ESI) available: [details of any supplementary information available should be included here]. See DOI: 00.0000/00000000.



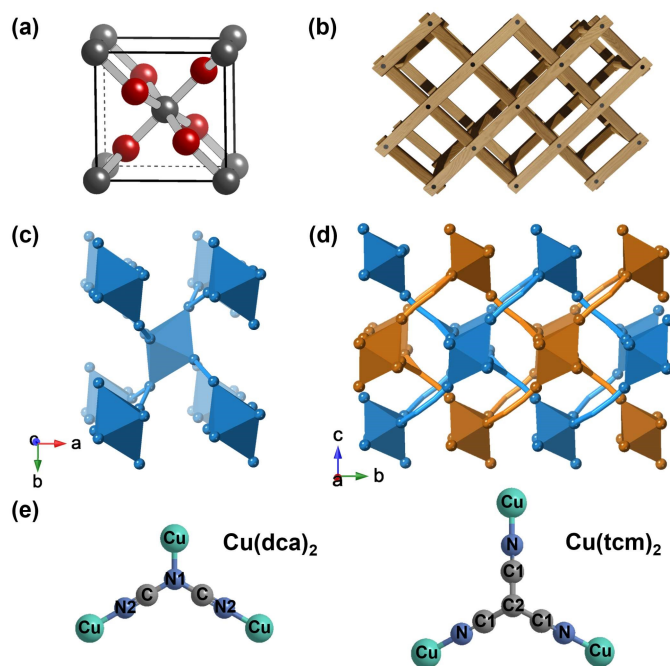


Fig. 1 (a) Unit cell of rutile (TiO<sub>2</sub>) structure.<sup>21</sup> (b) Schematic illustration of the "wine-rack" topology in rutile-structured solids. Crystal structures of (c) Cu(dca)<sub>2</sub> and (d) Cu(tcm)<sub>2</sub>, viewed along the *c*- and *a*-axes, respectively. The dca<sup>-</sup> and tcm<sup>-</sup> ligands are shown as simplified stick representations with carbon atoms omitted (C in Cu(dca)<sub>2</sub>); C1, C2 in Cu(tcm)<sub>2</sub> to better illustrate the network topology. All octahedra represent CuN<sub>6</sub> coordination environments. Cu(dca)<sub>2</sub> has a single rutile-like network, while Cu(tcm)<sub>2</sub> consists of two interpenetrating rutile-like networks distinguished by different colours. (e) Molecular structures and coordination modes of dca<sup>-</sup> and tcm<sup>-</sup> ligands with Cu<sup>2+</sup> centers.

tation within the framework, which spontaneously generates a symmetry-breaking strain.<sup>19</sup> When volume continuity is maintained during compression, the emergence of spontaneous strain can necessitate lengthening in at least one axial direction to stabilize the lower symmetry phase.<sup>20</sup> This elongation occurs because the material must compensate for contraction in other directions while preserving its overall volume, resulting in anisotropic deformation. Consequently, above the transition pressure, NLC is observed in such proper ferroelastic materials.

In addition to simple binary inorganic solids, the rutile topology has been reported in a variety of hybrid materials, in which the transition metal octahedra are connected by molecular linkers.<sup>22–24</sup> Transition metal dicyanamide and tricyanomethanide are two examples, abbreviated M(dca)<sub>2</sub> and M(tcm)<sub>2</sub> (M = Mn, Fe, Co, Ni, Cu).<sup>25</sup> M(dca)<sub>2</sub> exhibits a single rutile-like network in which the M<sup>2+</sup> cations are octahedrally coordinated to two dca<sup>-</sup> ligands via the nitrile and amide nitrogen donor atoms. In contrast, M(tcm)<sub>2</sub> exhibits a doubly interpenetrating structure with bonds exceeding 4.5 Å between the octahedral nodes (see Figure 1(e)).<sup>25</sup> These materials preferentially adopt CaCl<sub>2</sub>-type orthorhombic structures rather than rutile-type tetragonal structures at ambient conditions. Unlike rutile-structured dioxides and difluorides, M(dca)<sub>2</sub> and M(tcm)<sub>2</sub> do not undergo ferroelastic rutile-CaCl<sub>2</sub>-type phase transitions under pressure.

However, previous studies suggest that these materials still exhibit NLC behavior when subjected to external pressure.<sup>26,27</sup> A notable example is Co(dca)<sub>2</sub>, which exhibits NLC behavior with a value of  $-3.7(3)$  TPa<sup>-1</sup> over the pressure range of 0.05–1.11 GPa.<sup>27</sup> This NLC value is higher than those observed for binary inorganic solids with rutile topology—for instance, MgF<sub>2</sub> with  $K_{\text{NLC}} = -1.3(3)$  TPa<sup>-1</sup> and MnO<sub>2</sub> with  $K_{\text{NLC}} = -0.16(7)$  TPa<sup>-1</sup>.<sup>1,16</sup> This indicates that flexible molecular linkers enhance the responsiveness to external mechanical stimuli, leading to more pronounced structural changes.<sup>28</sup> Within the family of transition metal dicyanamides and tricyanomethanides, variations in the metal centers can significantly alter their mechanical properties. Factors such as ionic radius, electronic configuration, and coordination preferences can all influence the framework flexibility and thus the material's response to pressure.<sup>29</sup> An investigation of the relationship between chemical composition, crystal structure, and NLC properties within these materials is therefore particularly important for developing design principles for NLC materials.

This paper focuses on Cu(dca)<sub>2</sub> and Cu(tcm)<sub>2</sub>. These materials introduce additional structural complexity due to the Jahn–Teller distortion of their octahedral metal sites. Jahn–Teller distortion is a phenomenon that allows a degenerate electronic state to be deformed into a system of reduced symmetry. This transformation eliminates electronic degeneracy, thereby reducing energy levels.<sup>30</sup> Notably, a pronounced Jahn–Teller effect manifests in d<sup>9</sup> octahedral complexes, such as Cu(II).<sup>31</sup> This d<sup>9</sup> electronic configuration populates three electrons into two e<sub>g</sub> orbitals, resulting in a doubly degenerate ground state. To eliminate orbital and electronic degeneracy, Cu(II) complexes are deformed along the *z*-axis. However, the Jahn–Teller theorem does not dictate the direction of the distortion, but merely predicts the presence of an unstable geometry. Typically, the bonds to the ligands undergo stretching along the *z*-axis, although in certain cases they may instead shorten.<sup>32</sup>

For Cu(dca)<sub>2</sub> and Cu(tcm)<sub>2</sub>, a significant elongation of the Cu–N bond along the *z*-axis is observed. These elongated bonds, due to the Jahn–Teller effect, show a pronounced sensitivity to pressure. They are prone to rapid reduction upon compression.<sup>33</sup> Evidence for this phenomenon has been found in a number of coordination complexes with Cu<sup>2+</sup>. For example, Cu[Pt(CN)<sub>6</sub>] shows a higher compressibility along the *c*-axis ( $K_c = 15.3(2)$  TPa<sup>-1</sup>) compared to the *a*-axis ( $K_a = 4.82(11)$  TPa<sup>-1</sup>). This difference is attributed to the Jahn–Teller distorted bonds present along the *c*-axis.<sup>34,35</sup> With this in mind, we hypothesize that Jahn–Teller distortions could play a crucial role in enhancing the NLC properties of materials. The rapid compression in certain directions could be converted into substantial NLC behavior in the perpendicular direction via the hinge mechanism in wine-rack framework.

Here, the pressure-induced structural changes of Cu(dca)<sub>2</sub> and Cu(tcm)<sub>2</sub> are studied using high-pressure powder X-ray diffraction (HP-PXRD) and high-pressure powder neutron diffraction (HP-PNRD), respectively. The results reveal a remarkable NLC of  $-6.5(10)$  TPa<sup>-1</sup> along the *c*-axis over the pressure range of 0.05–1.11 GPa in the orthorhombic phase of Cu(dca)<sub>2</sub> (Cu(dca)<sub>2</sub>-I). Above 1.11 GPa, Cu(dca)<sub>2</sub> undergoes a phase transition from or-





thorhombic to monoclinic. It remains in the monoclinic phase,  $\text{Cu(dca)}_2\text{-II}$ , in the pressure range 1.11–3.06 GPa and shows no NLC behavior. In contrast to  $\text{Cu(dca)}_2$ ,  $\text{Cu(tcm)}_2$  maintains its orthorhombic structure over a wide pressure range of 0.05–3.75 GPa without undergoing any phase transition. It exhibits zero linear compressibility (ZLC) in the  $a$ -axis. Through an in-depth analysis of  $\text{Cu(dca)}_2$  and  $\text{Cu(tcm)}_2$ , and a comparative study with other rutile-like frameworks, we aim to elucidate the influence of three key factors on the magnitude of their NLC. These factors are (i) the framework topology, (ii) the unit cell density, and (iii) the electronic state of the metal cations. The interplay between these variables determines the magnitude of NLC in materials with rutile topology.

## 2 Experimental

**Synthesis:** Anhydrous  $\text{Cu(dca)}_2$  was synthesized according to the literature described synthesis procedure for  $\text{Mn(dca)}_2$ .<sup>36</sup> An 8 mL aqueous solution of Na(dca) (178.1 mg, 2 mmol) was added to a 2 mL aqueous solution of  $\text{Cu(NO}_3)_2 \cdot 3\text{H}_2\text{O}$  (241.6 mg, 1 mmol) with vigorous stirring, resulting in immediate precipitation of green-blue microcrystalline powder. To ensure complete reaction, the mixture was stirred for five minutes. The product was collected by filtration, washed with small amounts of deionized water and ethanol to remove impurities, and initially dried at 60 °C overnight. The powder was then heated under vacuum at 100 °C for 5 hours to yield anhydrous  $\text{Cu(dca)}_2$ .

$\text{Cu(tcm)}_2$  was synthesized according to the literature procedure.<sup>37</sup> A hot solution of K(tcm) (129.2 mg, 1 mmol) in water (4 mL) was added to a hot solution of  $\text{Cu(NO}_3)_2 \cdot 3\text{H}_2\text{O}$  (120.8 mg, 0.5 mmol) in water (3 mL). The solution was then allowed to cool while stirring continuously. A dark brown precipitate appeared some time after the solution reached room temperature. It was filtered, washed with deionized water and dried in an oven overnight (60 °C, 1 day).

**Structure characterization:** High-pressure powder X-ray diffraction (HP-PXRD) data of  $\text{Cu(dca)}_2$  were collected at beamline I15, Diamond Light Source, with an incident wavelength of 0.4246 Å (100×100 μm). A finely ground sample of  $\text{Cu(dca)}_2$  was loaded into a 500 μm hole of a steel gasket in a diamond anvil cell (DAC) with Daphne 7373 as the pressure transmitting medium (PTM) and a ruby sphere for pressure calibration. Pressure was determined by ruby fluorescence on-line at the beginning of each sequence using a Horiba iHR320 spectrometer (473 nm laser). The shift of the R1 fluorescence line of the ruby sphere was measured before and after each data collection, from which the experimental pressure could be calculated. At low pressures (< 1 GPa), the error of such measurements is small (typically 0.01 GPa) due to the minimisation of laser power and exposure time; at higher pressures (> 1 GPa), the standard error is usually assumed to be 0.1 GPa.  $\text{Cu(dca)}_2$  was measured at pressures ranging from 0.05 to 3.06 GPa. Diffraction images were collected with a Pilatus3 X CdTe 2M detector located approximately 230 mm from the sample and then integrated and corrected using DAWN software.<sup>38,39</sup> Lattice parameters and structural models were fitted to the data using the Rietveld module of the TOPAS software.<sup>40,41</sup>

For  $\text{Cu(tcm)}_2$ , HP-PXRD data were collected using a similar strategy at beamline ID27 at the European Synchrotron Radiation Facility (ESRF) over a pressure range of 0.02–0.86 GPa. Hydrostatic pressure was applied using a BETSA membrane diamond anvil cell (DAC) equipped with 600 μm Almax EasyLab type Ia Boehler-Almax design diamonds. A small amount (50×50 μm) of powder sample was loaded into the 300 μm diameter hole of a pre-impregnated stainless steel gasket. A small ruby sphere was also placed in the hole for pressure calibration using the ruby fluorescence method described above with silicon oil as the PTM. A wavelength of 0.3738 Å was used (beamsize 80×80 μm). Data were collected using a MARCCD detector with an approximate sample-to-detector distance of 306 mm, as calibrated using a  $\text{CeO}_2$  standard. Integration of 2D powder diffraction data was performed using DIOPAS v 2.4. Calibration, masking, and integration were consistent across all data sets.<sup>42</sup>

High-pressure powder neutron diffraction (HP-PNRD) data of  $\text{Cu(tcm)}_2$  were collected on the PEARL instrument at the ISIS neutron and muon source with a time-of-flight (ToF) transverse detector bank consisting of 9 modules and capable of observing  $d$ -spacings in the range 0.5–4.1 Å with a nominal average resolution of about 0.64%.<sup>43</sup> The  $\text{Cu(tcm)}_2$  powder sample was sealed in a zero scattering Ti-Zr gasket together with a Pb pressure marker and a mixture of pentane/isopentane as a pressure transmitting medium. The assembly was then loaded into zirconia-toughened alumina (ZTA) anvils and compression was applied using a Paris-Edinburgh (P-E) press. Measurements were made at pressures ranging from 0.05 to 3.75 GPa at room temperature.

## 3 Results and Discussion

$\text{Cu(dca)}_2$  has an orthorhombic structure under ambient conditions, constructed from  $\text{CuN}_6$  octahedra and trigonal  $\text{dca}^-$  linkers. A pronounced Jahn–Teller distortion occurs in the  $\text{CuN}_6$  octahedra due to the  $d^9$  electron configuration of the  $\text{Cu}^{2+}$  ions. This asymmetrical distortion is evidenced by significant bond length disparities; specifically, the axial Cu–N2 bond is elongated to 2.45 Å, while the equatorial Cu–N1 bond is considerably shorter at 1.92 Å. The axial Cu–N2 bond, oriented within the  $a$ – $b$  plane of the crystal structure, indicates potentially weaker bonding in this direction. This structural feature suggests a theoretical basis for rapid compression along the  $a$ - and  $b$ -axes of the crystal lattice under pressure. Our HP-PXRD study of  $\text{Cu(dca)}_2$  confirms this hypothesis, as shown in Figure 2.

Rietveld refinement of the HP-PXRD patterns shows that  $\text{Cu(dca)}_2$  preserves its initial orthorhombic phase, labelled  $\text{Cu(dca)}_2\text{-I}$ , over a pressure range from 0.05 to 1.11 GPa. Subsequently, a structural phase transition occurs, leading to a monoclinic phase,  $\text{Cu(dca)}_2\text{-II}$ , which persists up to pressures of 3.06 GPa. HP-PXRD patterns over these two phases are shown in Figure 2(a). The splitting of peaks beyond 1.11 GPa is indicative of this symmetry lowering process. The subtle volume discontinuity observed across the phase transition, as shown in Figure 2(c), indicates that this is a first-order transition. This phase transition is reversible. Upon pressure reduction, the compound reverts from the  $\text{Cu(dca)}_2\text{-II}$  phase back to its original orthorhombic configuration,  $\text{Cu(dca)}_2\text{-I}$  (See SI Figure S1).



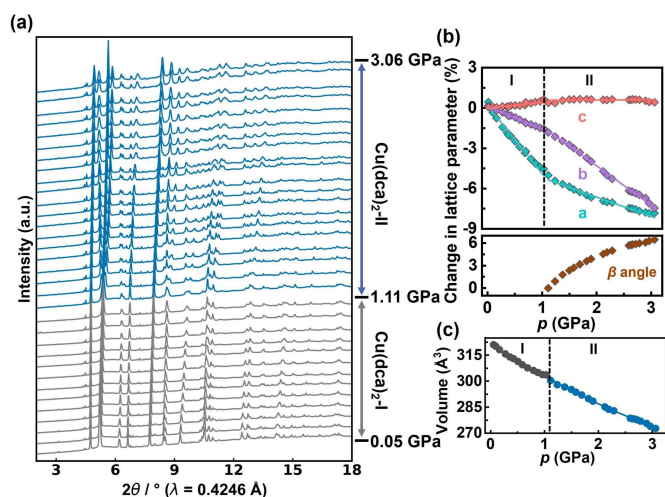


Fig. 2 (a) HP-PXRD patterns of Cu(dca)<sub>2</sub> in ascending order of pressure, illustrating the transition from orthorhombic to monoclinic phases. (b) Pressure-dependent evolution of Cu(dca)<sub>2</sub> lattice parameters shown as percentage changes from ambient pressure values, determined by HP-PXRD. The lattice parameters *a*, *b* and *c* are fitted separately with linear functions for the orthorhombic phase I (Cu(dca)<sub>2</sub>-I) and monoclinic phase II (Cu(dca)<sub>2</sub>-II) regions, while the  $\beta$  angle of phase II is fitted with a third-order polynomial equation. Error bars are within the size of the data points. (c) Unit cell volume of Cu(dca)<sub>2</sub> as a function of pressure. Grey points correspond to phase I and blue points to phase II. The data is fitted using the 2nd-order Birch–Murnaghan equation of state (BM EoS) using EoSFit7 GUI software.<sup>44</sup>

The lattice parameters of Cu(dca)<sub>2</sub> as a function of pressure are illustrated in Figure 2(b). For phase I, the lattice parameter *c* shows a progressive increase with increasing pressure, while lattice parameters *a* and *b* show systematic decreases, clearly demonstrating that Cu(dca)<sub>2</sub> undergoes pronounced anisotropic deformation under compression. The bulk modulus and uniaxial linear compressibility along each orthorhombic axis were determined for both phases of Cu(dca)<sub>2</sub> using EoSFit7 and PASCAL software, respectively.<sup>45,46</sup> It shows that Cu(dca)<sub>2</sub>-I exhibits positive linear compressibility (PLC) along the *a*- and *b*-axes and negative linear compressibility (NLC) along the *c*-axis, with values of 42.3(8) TPa<sup>−1</sup>, 16.5(9) TPa<sup>−1</sup> and −6.5(10) TPa<sup>−1</sup>, respectively, within the pressure range of 0.05 to 1.11 GPa. The calculated bulk modulus for Cu(dca)<sub>2</sub>-I is 14.9(4) GPa.

Cu(dca)<sub>2</sub>-II, while not exhibiting NLC behavior, also exhibits a minimum PLC along the *c* axis with a value of 7.1(8) TPa<sup>−1</sup> over the pressure range of 1.24 to 3.06 GPa; the corresponding PLC values along the *a*- and *b*-axes are 17.1(10) TPa<sup>−1</sup> and 30.7(8) TPa<sup>−1</sup>, respectively. The bulk modulus of Cu(dca)<sub>2</sub>-II is 12.3(3) GPa, which is lower than that of Cu(dca)<sub>2</sub>-I, indicating reduced mechanical stiffness after the phase transition. While this behavior is somewhat uncommon, it is not unprecedented and has been observed in other materials. For example, CrN exhibits an unexpected reduction of the bulk modulus of about 25% in the high-pressure orthorhombic phase compared to the low-pressure cubic phase at a transition pressure of  $\approx 1$  GPa.<sup>47</sup> Similarly, Cu<sub>2</sub>O shows a phenomenon where the monoclinic high-pressure phase has a bulk modulus of 41(6) GPa, which is three times softer

than the low-pressure cubic phase at 125(2) GPa.<sup>48</sup> In the case of Cu(dca)<sub>2</sub>, this reduced stiffness can be attributed to the lower symmetry in phase II, which allows greater degrees of freedom within the framework and consequently enables more substantial deformation under pressure.<sup>49</sup>

The key structural feature of Cu(dca)<sub>2</sub>-I that governs its anisotropic deformation under pressure is its “wine-rack” topology, illustrated in Figure 3(a). This distinctive network architecture exhibits pronounced compressibility along the *a*–*b* plane, which results from the presence of comparatively weaker, elongated Cu–N2 bonds. Through an efficient flexible hinge mechanism, this compression transforms into expansion along the perpendicular *c*-axis direction.<sup>50</sup> Detailed investigation of the structural deformation under pressure revealed an unexpected result: contrary to predictions, the Cu–N2 bond does not contract under pressure. As shown in Figure 3(e), this bond maintains nearly constant length throughout the pressure range of 0.05–1.9 GPa. Instead, Cu(dca)<sub>2</sub>-I exhibits significant octahedral distortion that coincides with compression of the unit cell along the *a*- and *b*-axes, as quantified by the parameter  $\phi$ . This parameter measures the deviation of the N1–Cu–N2 angle from the ideal 90°, and its evolution is shown in Figure 3(d). To determine  $\phi$ , the actual N1–Cu–N2 angle is calculated from the Rietveld refined structure and the difference from 90° is calculated according to Eq 1.

$$\phi = |\phi' - 90| \quad (1)$$

The observed octahedral distortion results from hinge-like tilting of the dca<sup>−</sup> ligands, which act as the ‘soft’ component of the framework, deforming to accommodate pressure-induced stress throughout the unit cell. Accompanying this tilting deformation, changes in the dca<sup>−</sup> ligand geometry are also evident. The dca<sup>−</sup> ligand, which consists of a cPoniform linkage with two C≡N1 bonds, undergoes deformation through modulation of its angle. As rapid compression occurs along the *a*- and *b*-axes, the dca<sup>−</sup> ligands flatten in these directions while simultaneously stretching along the perpendicular *c*-axis, thereby causing expansion of the unit cell in this direction. The angle  $\theta$  increases from 122.2(7) to 124.4(8)° over the pressure range of 0.0 to 1.03 GPa. These two coordinated deformation mechanisms—octahedral distortion and ligand deformation—appear to be the primary mechanisms responsible for negative linear compressibility in Cu(dca)<sub>2</sub>-I.

At 1.1 GPa, Cu(dca)<sub>2</sub> undergoes a structural transformation from an orthorhombic to a monoclinic phase. This phase transition introduces anisotropic character to the previously isotropic N1–C–N2–C–N1 bonds. Additionally, the angular parameter  $\phi$ , which indicates octahedral distortion, no longer increases systematically with pressure due to the enhanced structural complexity of Cu(dca)<sub>2</sub>-II. In this higher-pressure phase, Jahn–Teller bond contraction emerges as the primary deformation mechanism, exhibiting a multi-stage behavior. The Cu–N2 bond length shows distinct compression stages: initially remaining nearly constant from 0.05–1.9 GPa, followed by significant contraction of 0.16 Å between 1.9 and 2.7 GPa, and then leveling off at higher pressures, likely because other distortion mechanisms become dominant. However, due to the symmetry breaking and increased



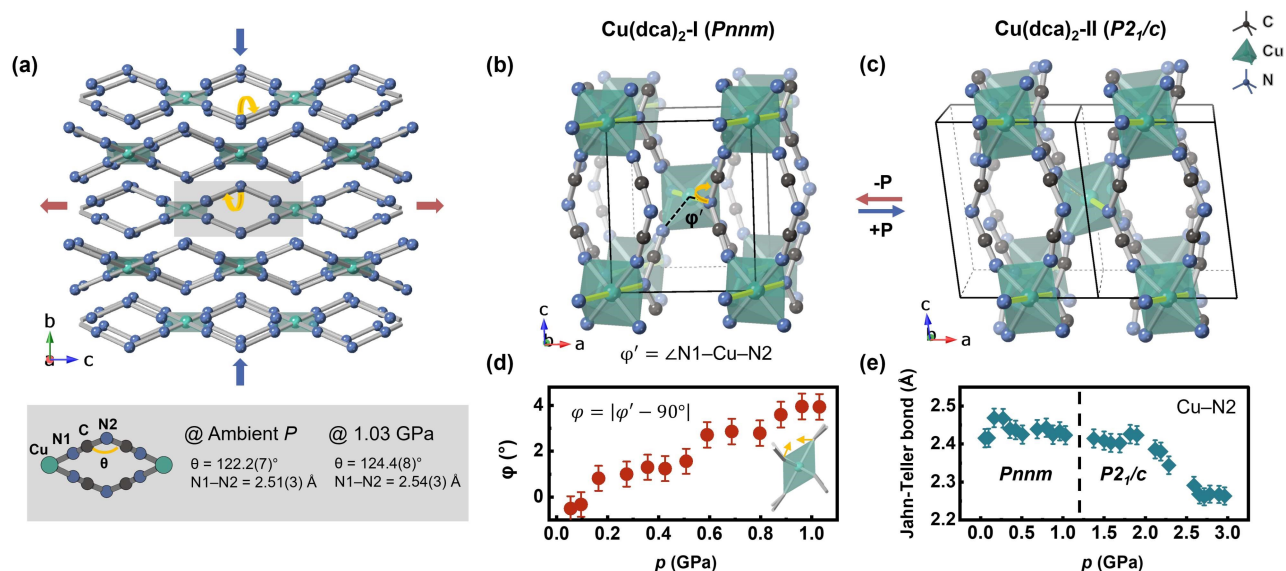


Fig. 3 Structural deformation mechanisms in  $\text{Cu(dca)}_2$  under pressure. (a) The "wine-rack" topology of  $\text{Cu(dca)}_2\text{-I}$ , with the axial Cu-N2 bonds omitted for clarity. This characteristic "wine-rack" motif governs the anisotropic deformation behavior under compression, driving rapid contraction along the  $a$ - and  $b$ -axes while simultaneously inducing expansion along the perpendicular  $c$ -axis. The bottom panel shows the  $\text{dca}^-$  ligand geometry and coordination mode, with the internal angle  $\theta$  increasing from  $122.2(7)^\circ$  at ambient pressure to  $124.4(8)^\circ$  at 1.03 GPa, illustrating the ligand deformation mechanism. (b) Crystal structure of  $\text{Cu(dca)}_2\text{-I}$  at 0.05 GPa and (c)  $\text{Cu(dca)}_2\text{-II}$  at 3.06 GPa, demonstrating the symmetry-breaking phase transition. The Jahn-Teller distorted Cu-N2 bonds are highlighted in yellow. During this transition, the terminal nitrogen atoms of the  $\text{dca}^-$  linkage become inequivalent, resulting in two distinct Cu-N1 bonds. (d) Evolution of the octahedral distortion parameter  $\varphi$  with increasing pressure, where  $\varphi$  quantifies the deviation of the N1-Cu-N2 angle from  $90^\circ$ . (e) Pressure-dependent behavior of the long Jahn-Teller-distorted Cu-N2 bond length over the studied pressure range.

number of crystallographically distinct sites in the low-symmetry monoclinic structure, it is challenging to establish clear correlations between different deformation mechanisms and identify distinct pressure regimes. These observations suggest that  $\text{Cu(dca)}_2\text{-II}$ , which possesses a denser structure than  $\text{Cu(dca)}_2\text{-I}$ , accommodates compression primarily through contraction of Jahn-Teller bonds in the pressure range of 1.9–2.7 GPa. This deformation mechanism differs from that observed in  $\text{Cu(dca)}_2\text{-I}$ , where deformation occurs through tilting of the binding ligands within the more spacious intra-framework voids. Despite its denser packing,  $\text{Cu(dca)}_2\text{-II}$  exhibits a lower bulk modulus than  $\text{Cu(dca)}_2\text{-I}$ , indicating a more compliant structure. This softening can be attributed to the loss of the directional rigidity that characterizes phase I along the  $c$ -axis, combined with the reduced symmetry in phase II, which allows greater degrees of freedom within the framework and consequently enables more substantial deformation under pressure.

$\text{Cu(tcm)}_2$ , like  $\text{Cu(dca)}_2$ , has a rutile-like coordination framework. This compound consists of octahedral  $\text{Cu}^{2+}$  cations and trigonal  $\text{tcm}^-$  anions. Under ambient conditions,  $\text{Cu(tcm)}_2$  shows an orthorhombic structure with space group  $Pmna$ . A characteristic Jahn-Teller distortion is observed, with the Jahn-Teller axis lying within the  $b$ - $c$  plane, leading to an elongation of the axial Cu-N2 bonds by  $0.47 \text{ \AA}$  with respect to their equatorial Cu-N1 counterparts. Despite these similarities,  $\text{Cu(tcm)}_2$  differs from  $\text{Cu(dca)}_2$  in terms of its structural arrangement. It has a doubly interpenetrating structure, as opposed to the single network seen in  $\text{Cu(dca)}_2$ . This interpenetration arises from the

increased distance between the octahedral nodes in  $\text{Cu(tcm)}_2$ . Within  $\text{Cu(tcm)}_2$ ,  $\text{Cu}^{2+}$  cations are separated by extended paths of 5 atoms (N-C1-C2-C1-N). Conversely,  $\text{Cu(dca)}_2$  features two distinct pathways between the Cu centers, namely N1-C-N2-C-N1 and N1-C-N2 with chains of 5 and 3 atoms, respectively. While the 5-atom pathway matches the length of the connections in  $\text{Cu(tcm)}_2$ , the shorter 3-atom connection in  $\text{Cu(dca)}_2$  significantly reduces the void space, thereby restricting the potential for interpenetration.<sup>37</sup>

Rietveld refinement of HP-PNRD patterns reveals that  $\text{Cu(tcm)}_2$  maintains its orthorhombic structure at ambient conditions and over a wide pressure range of 0–3.75 GPa (see Figure 4 and Figure S4 in SI). The bulk modulus of  $\text{Cu(tcm)}_2$  within this pressure range is  $24.5(4) \text{ GPa}$ , significantly higher than that of  $\text{Cu(dca)}_2\text{-I}$ , which is  $14.9(4) \text{ GPa}$  over 0.05–1.11 GPa. This higher modulus indicates greater stiffness of the former, enabling it to retain its initial structure under extreme conditions, but limiting its structural response to applied pressure. Regarding lattice deformation under pressure,  $\text{Cu(tcm)}_2$  exhibits positive linear compressibility (PLC) along the  $c$ -axis of  $29.6(4) \text{ TPa}^{-1}$  and along the  $b$ -axis of  $1.1(3) \text{ TPa}^{-1}$ . It also displays zero linear compressibility (ZLC) along the  $a$ -axis with a value of  $-0.1(2) \text{ TPa}^{-1}$ . Unlike  $\text{Cu(dca)}_2$ , the compound does not show substantial negative linear compressibility. Instead, it exhibits stable ZLC behavior along the  $a$ -axis and very small PLC of  $1.1(3) \text{ TPa}^{-1}$  along the  $b$ -axis over a wide pressure range. This combination results in a near-zero area compression in the  $a$ - $b$  plane of  $1.0(5) \text{ TPa}^{-1}$ , a property rarely observed in materials.<sup>51</sup> Such exceptional mechanical behavior,



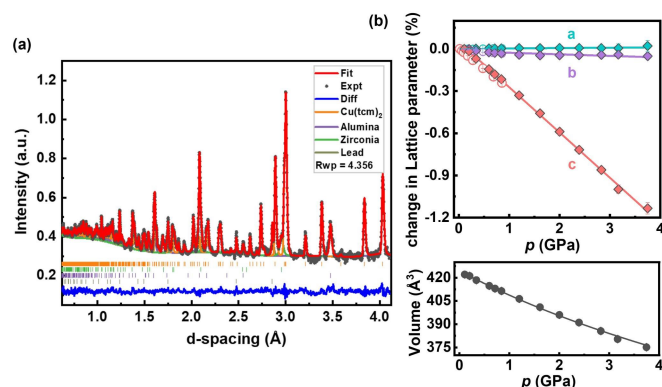


Fig. 4 (a) Neutron diffraction pattern of  $\text{Cu}(\text{tcm})_2$  at 0.11 GPa, fitted using Rietveld refinement. The experimental data are displayed in black, the fit in red, and the residuals in blue. The calculated signals for alumina, zirconia, and lead, which come from anvil and pressure marker, are represented by purple, green, and dark green lines, respectively, while the permitted reflections for each phase are represented by vertical bars. The excellent visual agreement demonstrates the quality of the refinement. (b) Variation of the lattice parameters of  $\text{Cu}(\text{tcm})_2$  in response to increasing pressure. The HP-PNRD and HP-PXRD data points are represented by solid and open diamonds, respectively. The lattice parameters are linearly fitted while the volume data is fitted using the 2nd-order Birch–Murnaghan equation of state (BM EoS) using EoSFit7 GUI software.<sup>44</sup>

with compression along the  $c$ -axis while maintaining near-zero area compression in the  $a$ – $b$  plane, makes  $\text{Cu}(\text{tcm})_2$  promising for potential applications in ultrasensitive pressure sensors and actuators where directional mechanical response is desirable.<sup>52</sup>

Although octahedral and  $\text{dca}^-$  ligand distortions are major pressure-induced deformations influencing NLC behavior in  $\text{Cu}(\text{dca})_2$ , these phenomena are not detected in  $\text{Cu}(\text{tcm})_2$ . This discrepancy is due to the combined effects of spatial constraints within the framework and the inherent rigidity of the ligands in the latter compound. On the one hand, the doubly interpenetrating network structure of  $\text{Cu}(\text{tcm})_2$  increases the density, thereby preventing any potential ligand tilt-induced octahedral distortion. On the other hand, the coordination geometry of  $\text{tcm}^-$  ligands limits the extent of flexibility found in  $\text{Cu}(\text{dca})_2$ . In contrast to  $\text{dca}^-$ ,  $\text{tcm}^-$  possesses a planar, trigonal geometry that is notably rigid. Its interaction with metal centers occurs strictly through its terminal nitrogen donors. This stable trigonal geometry enables  $\text{tcm}^-$  to maintain its structural integrity under compression, resisting distortion of its internal geometry.

The pronounced anisotropic deformation in  $\text{Cu}(\text{tcm})_2$  is driven by compaction of interpenetrating networks and Jahn–Teller bonds. As shown in Figure 5, the interpenetrating structure has an architectural feature with substantial intraframework space along the  $c$ -axis, which facilitates rapid contraction of the unit cell along this axis under pressure. The extent of deformation within the  $\text{Cu}(\text{tcm})_2$  crystal structure is characterized by the variation in the torsion angle  $\theta$ , which measures the twist between two opposing planes of planar  $\text{tcm}^-$  ions within the two interpenetrating networks. The value of  $\theta$  is influenced by both the distance between the two interpenetrating networks and changes in the  $a$  lattice parameter. Throughout the pressure range, the de-

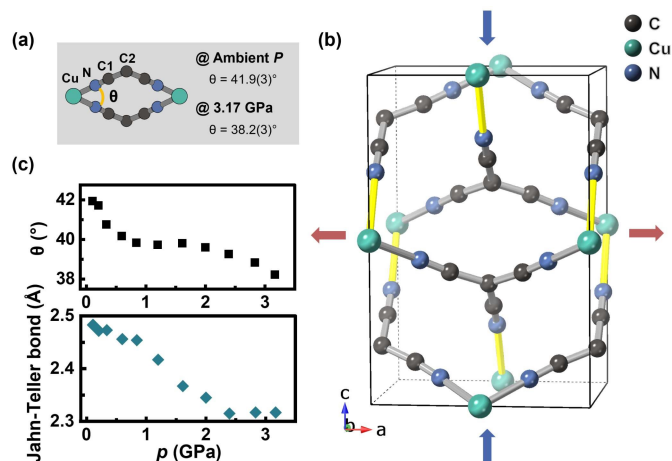


Fig. 5 Pressure-induced structural deformation mechanisms in  $\text{Cu}(\text{tcm})_2$ . (a) Local coordination environment showing the Cu center and  $\text{tcm}^-$  ligand with the inter-network torsion angle  $\theta$  at ambient pressure and 3.17 GPa. (b) Crystal structure viewed along the  $a$ -axis, showing the doubly interpenetrating rutile-like networks. The Jahn–Teller distorted Cu–N bonds are highlighted in yellow. (c) Pressure dependence of the inter-network torsion angle  $\theta$  and Jahn–Teller bond length, demonstrating the multi-stage deformation behavior under compression.

formation exhibits a multi-stage mechanism in  $\theta$ , correlating with pressure increase and suggesting a closer approach of the two interpenetrating networks. Analysis reveals three distinct compression stages: (i) 0–1 GPa, where compression occurs primarily via the angle  $\theta$ ; (ii) 1–2.5 GPa, where deformation is dominated by Jahn–Teller bond contraction; and (iii) above 2.5 GPa, where the torsion angle mechanism becomes dominant again. Furthermore, the Jahn–Teller-distorted long bond in  $\text{Cu}(\text{tcm})_2$ , located in the  $b$ – $c$  plane, contributes to the overall compressibility. Characterized by its length and relative weakness, this bond consistently contracts upon compression, a behavior evident in Figure 5, and shows a leveling off at approximately 2.5 GPa. This multi-stage compression behavior is similar to that observed in  $\text{Cu}(\text{dca})_2$ -II, where different deformation mechanisms dominate at different pressure ranges. The  $c$ -axis of  $\text{Cu}(\text{tcm})_2$  is connected to the  $a$ -axis via a ‘wine-rack’ packing of atoms. This configuration enables the efficient transformation of rapid compression along the  $c$ -axis into expansion in the perpendicular directions. As a result, ZLC is observed along the  $a$ -axis. Similarly, the negligible positive linear compressibility (PLC) magnitude along the  $b$ -axis can be interpreted as a consequential effect of the network’s compression-induced reconfiguration along the  $c$ -axis.

## 4 Conclusion

In conclusion,  $\text{Cu}(\text{dca})_2$  and  $\text{Cu}(\text{tcm})_2$ , as structural analogues of rutile, both display anisotropic compression behavior, though to varying degrees. Specifically,  $\text{Cu}(\text{dca})_2$  demonstrates a pronounced negative linear compressibility (NLC) of  $-6.5(10) \text{ TPa}^{-1}$  along the  $c$ -axis across a pressure range of 0.05 to 1.11 GPa. By contrast,  $\text{Cu}(\text{tcm})_2$  shows zero linear compressibility (ZLC) with a magnitude of  $-0.1(2) \text{ TPa}^{-1}$  along the  $a$ -axis, maintained over a wider pressure range from 0 to 3.75 GPa. The appearance of NLC/ZLC behavior in these compounds can be attributed to



their 'wine-rack' topology, which effectively translates rapid compression in one direction into expansion in the perpendicular direction. The differences in compressibility magnitudes between these two compounds can be explained by considering the disparities in their connecting ligands and structural configurations.  $\text{Cu(dca)}_2$  features a single rutile-like structure formed by flexible  $\text{dca}^-$  ligands. This structure, compared to the interpenetrating architecture of  $\text{Cu(tcm)}_2$  linked by rigid  $\text{tcm}^-$  ligands, undergoes more pronounced deformation upon compression. This results in a greater magnitude of NLC but also a more rapid structural collapse. Furthermore,  $\text{Cu(dca)}_2$  undergoes a first-order phase transition from an orthorhombic to a monoclinic structure above 1.11 GPa. Conversely,  $\text{Cu(tcm)}_2$  retains its initial orthorhombic structure over the entire pressure range without undergoing any phase transition.

Both  $\text{Cu(dca)}_2$  and  $\text{Cu(tcm)}_2$  exhibit a notable elongation of the Cu–N2 bonds, attributed to the Jahn–Teller effect. However, their responses to compression vary distinctly. Specifically,  $\text{Cu(tcm)}_2$  undergoes a considerable Cu–N2 bond contraction when compressed, a feature not observed in  $\text{Cu(dca)}_2$ . This discrepancy arises from the flexibility of the  $\text{dca}^-$  ligands present in  $\text{Cu(dca)}_2$ , which deform to accommodate compressive stress, preventing the bonds from contracting. Although  $\text{Cu(dca)}_2$  does not demonstrate direct Jahn–Teller bond contraction, the effect nevertheless plays a critical role in this compound. The Jahn–Teller distortion creates anisotropic coordination environments that generate considerable intraframework space along the  $a$ - and  $b$ -axes, facilitating the deformation of the  $\text{dca}^-$  ligands. This process enhances the compressibility along these axes, further emphasizing the NLC behavior of  $\text{Cu(dca)}_2$  under pressure.

The predominant pressure-induced deformations in  $\text{Cu(dca)}_2$  and  $\text{Cu(tcm)}_2$  differ significantly. For  $\text{Cu(dca)}_2$ -I, the main changes are octahedral and  $\text{dca}^-$  ligand distortions, whereas  $\text{Cu(tcm)}_2$  primarily undergoes compaction of interpenetrating networks and Jahn–Teller bond contraction. This variance underlines the distinct structural responses of these copper compounds under pressure, demonstrating the diversity of their physical properties despite their shared rutile-like topology.

These findings establish important design principles for engineering NLC materials. The interplay between three key factors emerges as crucial: (i) framework topology (wine-rack motif with single vs. interpenetrating networks), (ii) ligand flexibility (flexible  $\text{dca}^-$  vs. rigid  $\text{tcm}^-$ ), and (iii) electronic effects (Jahn–Teller distortion). The  $\text{Cu(dca)}_2$  system demonstrates that combining flexible ligands with Jahn–Teller-active metal centers in a single wine-rack network topology can achieve NLC values ( $-6.5 \text{ TPa}^{-1}$ ) that are significantly higher than conventional inorganic rutile materials (typically  $< 2 \text{ TPa}^{-1}$ ), while  $\text{Cu(tcm)}_2$  shows ZLC and near-zero area compressibility phenomenon with exceptional stability over wide pressure ranges. These insights provide a rational framework for designing next-generation mechanical metamaterials with tailored compressibility responses, potentially advancing applications in pressure-resistant optical devices, ultrasensitive sensors, and mechanical actuators where precise directional responses are essential.

## Author Contributions

M.C.: Conceptualization, Methodology, Investigation, Formal analysis, Writing – original draft. H.L.B.B.: Investigation, Writing – review & editing. D.D.: Investigation, Writing – review & editing. N.P.F.: Investigation, Writing – review & editing. C.J.R.: Investigation, Writing – review & editing. A.B.C.: Supervision, Project administration, Funding acquisition, Writing – review & editing.

## Conflicts of interest

There are no conflicts to declare.

## Acknowledgements

We thank the Science and Technology Facilities Council ISIS Neutron and Muon Source (STFC ISIS Facility) (data DOI: 10.5286/ISIS.E.RB2010698) and the Diamond Light Source (proposal number CY29285) for the provision of beamtime. We thank the European Synchrotron Radiation Facility (ESRF) for providing beamtime through ABC's postdoctoral fellowship. HLBB acknowledges financial support from the Swedish Research Council (VR, grant number 2022-02984) and the Wallenberg Initiative Materials Science for Sustainability (WISE), funded by the Knut and Alice Wallenberg Foundation.

## Notes and references

- 1 A. B. Cairns and A. L. Goodwin, *Physical Chemistry Chemical Physics*, 2015, **17**, 20449–20465.
- 2 R. H. Baughman, S. Stafstrom, C. Cui and S. O. Dantas, *Science*, 1998, **279**, 1522–1524.
- 3 I. Loa, K. Syassen, R. Kremer, U. Schwarz and M. Hanfland, *Physical Review B*, 1999, **60**, R6945.
- 4 A. B. Cairns, A. L. Thompson, M. G. Tucker, J. Haines and A. L. Goodwin, *Journal of the American Chemical Society*, 2012, **134**, 4454–4456.
- 5 P. Serra-Crespo, A. Dikhtiarenko, E. Stavitski, J. Juan-Alcañiz, F. Kapteijn, F.-X. Coudert and J. Gascon, *CrystEngComm*, 2015, **17**, 276–280.
- 6 Q. Zeng, K. Wang and B. Zou, *Journal of the American Chemical Society*, 2017, **139**, 15648–15651.
- 7 M. Chen, H. L. B. Boström, D. Daisenberger, N. P. Funnell, C. J. Ridley, M. Mezouar, C. Weidenthaler and A. B. Cairns, *Journal of the American Chemical Society*, 2025.
- 8 A. B. Cairns, J. Catafesta, C. Levelut, J. Rouquette, A. Van Der Lee, L. Peters, A. L. Thompson, V. Dmitriev, J. Haines and A. L. Goodwin, *Nature materials*, 2013, **12**, 212–216.
- 9 A. L. Goodwin, D. A. Keen and M. G. Tucker, *Proceedings of the National Academy of Sciences*, 2008, **105**, 18708–18713.
- 10 Z. Hiroi, *Inorganic Chemistry*, 2022, **61**, 8393–8401.
- 11 W. H. Baur and A. A. Khan, *Acta Crystallographica Section B: Structural Crystallography and Crystal Chemistry*, 1971, **27**, 2133–2139.
- 12 J. Haines, J. Léger and S. Hoyau, *Journal of Physics and Chemistry of Solids*, 1995, **56**, 965–973.





- 13 P. Peeroy, I. Fritz and G. Samara, *Journal of Physics and Chemistry of Solids*, 1975, **36**, 1105–1122.
- 14 J. Haines, J. M. Leger, C. Chateau and A. S. Pereira, *Physics and Chemistry of Minerals*, 2000, **27**, 575–582.
- 15 S. López-Moreno, A. Romero, J. Mejía-López, A. Muñoz and I. V. Roshchin, *Physical Review B—Condensed Matter and Materials Physics*, 2012, **85**, 134110.
- 16 L. Ming, M. Manghnani, T. Matsui and J. Jamieson, *Physics of the Earth and Planetary Interiors*, 1980, **23**, 276–285.
- 17 J. Haines and J. Léger, *Physical Review B*, 1997, **55**, 11144.
- 18 E. K. Salje, *Annual Review of Materials Research*, 2012, **42**, 265–283.
- 19 A. Togo, F. Oba and I. Tanaka, *Physical Review B*, 2008, **78**, 134106.
- 20 E. Salje, *Ferroelectrics*, 1990, **104**, 111–120.
- 21 R. W. G. Wyckoff and R. W. Wyckoff, *Crystal structures*, Interscience publishers New York, 1963, vol. 1.
- 22 C. Qin, X.-L. Wang, E.-B. Wang and Z.-M. Su, *Inorganic chemistry*, 2005, **44**, 7122–7129.
- 23 J.-L. Niu, G.-X. Hao, J. Lin, X.-B. He, P. Sathishkumar, X.-M. Lin and Y.-P. Cai, *Inorganic chemistry*, 2017, **56**, 9966–9972.
- 24 R. Abazari, E. Yazdani, M. Nadafan, A. M. Kirillov, J. Gao, A. M. Slawin and C. L. Carpenter-Warren, *Inorganic Chemistry*, 2021, **60**, 9700–9708.
- 25 S. R. Batten and K. S. Murray, *Coordination Chemistry Reviews*, 2003, **246**, 103–130.
- 26 X. Fan, T. Yan, Q. Wang, J. Zheng, Z. Ma and Z. Xue, *Chemistry Letters*, 2019, **48**, 1375–1378.
- 27 A. A. Yakovenko, K. W. Chapman and G. J. Halder, *Acta Crystallographica Section B: Structural Science, Crystal Engineering and Materials*, 2015, **71**, 252–257.
- 28 W. Cai, A. Gładysiak, M. Anioła, V. J. Smith, L. J. Barbour and A. Katrusiak, *Journal of the American Chemical Society*, 2015, **137**, 9296–9301.
- 29 J. L. Korcok, M. J. Katz and D. B. Leznoff, *Journal of the American Chemical Society*, 2009, **131**, 4866–4871.
- 30 P. R. Bunker and P. Jensen, *Molecular symmetry and spectroscopy*, NRC research press, 2006, vol. 46853.
- 31 D. F. Shriver and P. Atkins, *Inorganic Chemistry*, [Publisher needed], 3rd edn, 1999.
- 32 R. Janes, *Metal-ligand bonding*, Royal Society of Chemistry, Cambridge, 2004.
- 33 H. L. B. Boström, A. B. Cairns, M. Chen, D. Daisenberger, C. J. Ridley and N. P. Funnell, *Chemical Science*, 2024, **15**, 3155–3164.
- 34 H. L. Boström, I. E. Collings, A. B. Cairns, C. P. Romao and A. L. Goodwin, *Dalton Transactions*, 2019, **48**, 1647–1655.
- 35 I. E. Collings, M. Bykov, E. Bykova, M. Hanfland, S. van Smaalen, L. Dubrovinsky and N. Dubrovinskaia, *CrystEngComm*, 2018, **20**, 3512–3521.
- 36 C. R. Kmety, Q. Huang, J. W. Lynn, R. W. Erwin, J. L. Manson, S. McCall, J. Crow, K. L. Stevenson, J. S. Miller and A. J. Epstein, *Physical Review B*, 2000, **62**, 5576.
- 37 S. Batten, B. Hoskins, K. Murray *et al.*, *Journal of the Chemical Society, Dalton Transactions*, 1999, 2977–2986.
- 38 M. Basham, J. Filik, M. T. Wharmby, P. C. Chang, B. El Kassaby, M. Gerring, J. Aishima, K. Levik, B. C. Pulford, I. Sikharulidze *et al.*, *Journal of synchrotron radiation*, 2015, **22**, 853–858.
- 39 J. Filik, A. Ashton, P. Chang, P. Chater, S. Day, M. Drakopoulos, M. Gerring, M. Hart, O. Magdysyuk, S. Michalik *et al.*, *Journal of applied crystallography*, 2017, **50**, 959–966.
- 40 H. Rietveld, *Acta Crystallographica*, 1967, **22**, 151–152.
- 41 A. A. Coelho, *Journal of Applied Crystallography*, 2018, **51**, 210–218.
- 42 C. Prescher and V. B. Prakapenka, *High Pressure Research*, 2015, **35**, 223–230.
- 43 C. Bull, N. Funnell, M. Tucker, S. Hull, D. Francis and W. Marshall, *High Pressure Research*, 2016, **36**, 493–511.
- 44 R. J. Angel, M. Alvaro and J. Gonzalez-Platas, *Zeitschrift für Kristallographie-Crystalline Materials*, 2014, **229**, 405–419.
- 45 J. Gonzalez-Platas, M. Alvaro, F. Nestola and R. Angel, *Journal of Applied Crystallography*, 2016, **49**, 1377–1382.
- 46 M. J. Cliffe and A. L. Goodwin, *Journal of Applied Crystallography*, 2012, **45**, 1321–1329.
- 47 F. Rivadulla, M. Bañobre-López, C. X. Quintela, A. Piñeiro, V. Pardo, D. Baldomir, M. A. López-Quintela, J. Rivas, C. A. Ramos, H. Salva, J.-S. Zhou and J. B. Goodenough, *Nature Materials*, 2009, **8**, 947–951.
- 48 F. Qin, D. Zhang and S. Qin, *Frontiers in Earth Science*, 2021, **9**, 740685.
- 49 H. Fang and M. T. Dove, *Physical Review B*, 2013, **87**, 214109.
- 50 R. E. Newnham, *Properties of materials: anisotropy, symmetry, structure*, Oxford University Press on Demand, 2005.
- 51 D. Jiang, T. Wen, H. Song, Z. Jiang, C. Li, K. Liu, W. Yang, H. Mao and Y. Wang, *CCS Chemistry*, 2022, **4**, 3246–3253.
- 52 Q. Zeng, K. Wang and B. Zou, *ACS Applied Materials & Interfaces*, 2018, **10**, 23481–23484.



The data supporting this article have been included as part of the Supplementary Information.

[View Article Online](#)  
DOI: 10.1039/D5SC04854K

